Journal of Nuclear Materials xxx (xxxx) xxx

Contents lists available at ScienceDirect

Journal of Nuclear Materials

journal homepage: www.elsevier.com/locate/jnucmat

Evaluating the microstructure and origin of nonmetallic inclusions in as-cast U-10Mo fuel

Elizabeth J. Kautz [1,#,*], Sina Shahrezaei [1,#], Matthew Athon [2], Michael Frank [3], Alan Schemer-Kohrn [1], Ayoub Soulami [4], Curt Lavender [1], Vineet V. Joshi [1], Arun Devaraj [4,*]

[1] Energy and Environment Directorate, Pacific Northwest National Laboratory, Richland, WA 99354 USA
[2] National Security Directorate, Pacific Northwest National Laboratory, Richland, WA 99354 USA
[3] Department of Material Science and Engineering, University of North Texas, Denton, TX 76207
[4] Physical and Computational Sciences Directorate, Pacific Northwest National Laboratory, Richland, WA 99354 USA

ARTICLE INFO

Article history:
Received 27 November 2020
Revised 13 February 2021
Accepted 15 March 2021
Available online xxx

Keywords:
Casting
metallic nuclear fuel
U-10Mo
uranium-molybdenum
low-enriched uranium
LEU
atom probe tomography

ABSTRACT

Low enriched uranium alloyed with 10 wt. % molybdenum (U-10Mo) has been identified as a promising alternative to highly enriched uranium oxide dispersion fuels for use in high performance research and test reactors. Manufacturing U-10Mo alloy fuel involves several complex thermomechanical processing steps and understanding of the microstructure and its evolution throughout the various fabrication steps is critical to enable the deployment of a reliable fuel production capability. Nonmetallic inclusions are often found in U castings and may affect subsequent fuel processing steps and microstructure evolution. Yet, the origin of these inclusions is not well established. To elucidate their origin and formation mechanisms, nonmetallic inclusions in U-10Mo castings were characterized on sub-nanometer to millimeter scale. Inclusion distribution, morphology, size, and composition were determined for the metallic fuel samples. Inclusions were estimated to comprise ~ 0.4 % of the fuel (by area), were identified at both grain boundaries and grain interiors, and were found to have varying morphologies (e.g., core-shell, elongated, blocky). All inclusions were either uranium carbides or oxides, or a combination of the two (i.e., dual-phase inclusions). Analysis of inclusions via atom probe tomography revealed that carbides and oxides were hypostoichiometric, with minor amounts of additional impurity elements present (e.g., Si, H). All analyzed inclusions were found to be enriched to ~20 at. % ^{235}U, consistent with the surrounding γ-UMo matrix and target enrichment for the low enriched U fuel, indicating that the inclusions formed during the downblending of highly enriched U metal with depleted U via the melting and casting processes.

© 2021 Elsevier B.V. All rights reserved.

1. Introduction

Metallic nuclear fuels have been studied extensively since the 1940s for use in commercial and research reactors due to their more favorable machinability, higher uranium (U) density and improved thermal conductivity as compared to the more traditional ceramic or dispersion systems [1-3]. Metallic fuels are typically U alloys that maintain a high fissile density of ^{235}U, with better chemical and mechanical properties than unalloyed U [4,5]. High assay low-enriched U (LEU) nuclear fuels (i.e., 5 wt. % < ^{235}U < 20 wt. %) are currently being developed to replace highly enriched uranium (HEU) oxide dispersion fuels, to reduce the significant proliferation risks associated with continued HEU operations [6]. LEU alloyed with 10 wt. % molybdenum (U-10Mo) in a plate-type (i.e., monolithic) design is a leading LEU fuel candidate, particularly for the United States high-performance research reactors, because a high ^{235}U density is possible [6]. Alloying U with 10 wt. % Mo stabilizes the high-temperature γ-UMo phase with body-centered cubic structure, which provides isotropic properties or behavior (e.g., swelling in an irradiation environment) unlike other U allotropes [7-9]. In addition, U-10Mo provides reasonable corrosion resistance, ductility, and fracture toughness for application in an operating reactor environment [4,10,11]. In order to deploy a reliable production capability, the evolution of U-10Mo microstructure throughout the fabrication process must be well understood. Inhomogeneities in the as-cast microstructure (e.g., Mo segregation, and morphology and elemental/isotopic composition of nonmetallic inclusions) can directly affect microstructure evolution in subse-

* Corresponding authors.
E-mail addresses: elizabeth.kautz@pnnl.gov (E.J. Kautz), arun.devaraj@pnnl.gov (A. Devaraj).
# These authors contributed equally to this work

https://doi.org/10.1016/j.jnucmat.2021.152949
0022-3115/© 2021 Elsevier B.V. All rights reserved.

Please cite this article as: E.J. Kautz, S. Shahrezaei, M. Athon et al., Evaluating the microstructure and origin of nonmetallic inclusions in as-cast U-10Mo fuel, Journal of Nuclear Materials, https://doi.org/10.1016/j.jnucmat.2021.152949

quent processing steps and fuel performance in an irradiation environment.

Nonmetallic inclusions and impurity elements have previously been identified in manufactured U-10Mo fuels, including UC and U_2MoSi_2C [12,13], yet their enrichment and origin have only recently been investigated [14,15]. Inclusions and impurity elements are present in the feedstock material, but may also be picked up from the environment during casting (i.e., melt interaction with the crucible and/or casting atmosphere). Intrinsic impurity phases in depleted uranium (DU) or HEU feedstock materials that do not dissolve in the liquid phase field at 1673 K (~1400 ^{0}C) would retain their original U isotopic signature after casting, which would indicate that the inclusions originated from feedstock materials. On the other hand, if feedstock impurity phases dissolve completely, then carbides, oxides, or variants (e.g., oxycarbides) could precipitate during the casting process [16,17]. Isotopic enrichment of the nonmetallic inclusions that is very different from the LEU specification can directly affect irradiation performance by leading to nonuniform fission density (and thus nonuniform temperature and fission product formation) in the fuel [18]. While the effects of homogenization and thermomechanical processing on the kinetics of grain growth and phase transformations have been studied [19-21], the starting (i.e., as-cast) microstructure, and in particular the role and origin of nonmetallic inclusions, is not well understood. The presence of nonmetallic inclusions may influence grain growth and the local phase transformation kinetics during downstream fuel processing [13,22]. In addition, second-phase particles dispersed in a polycrystalline material can affect microstructure evolution during subsequent annealing and hot/cold rolling [23-25]. Hence, detailed understanding of inclusion characteristics (e.g., distribution, size, morphology) can help to advance the computational models that detail phenomena such as particle-assisted abnormal grain growth and particle pinning [22,26], and allow for better predictions of microstructure-processing relationships.

In this work, a multimodal, multi-length-scale approach was applied to investigate the as-cast U-10Mo microstructure. Grain size, morphology, and distribution of nonmetallic inclusions were characterized in two fuel plates via optical and scanning electron microscopy. To further detail the elemental distribution across inclusions at different locations in U-10Mo castings, scanning electron microscope energy dispersive x-ray spectroscopy (SEM-EDS) mapping was employed. For a subset of fine-scale inclusions, atom probe tomography (APT) was performed to investigate nanoscale morphology of inclusions and to identify their elemental and isotopic compositions in comparison with the surrounding matrix. The combination of these techniques provides insight into fuel plate processing history and the origins of nonmetallic inclusions.

2. Materials and Methods

DU, HEU, and Mo were mixed in proportions to meet the target U enrichment (~ 20 wt. % ^{235}U) and the 10 wt. % Mo alloying specification. Raw materials were vacuum induction melted and cast into ingots at the Y12 National Security Complex. The melt was held at 1673 K (~1400°C) for 30 minutes, then poured into a preheated Er_2O_3-coated graphite crucible. The melt was then furnace-cooled to ~600°C and air-cooled to room temperature. Each vertical melt pour yielded three parallel cast plates which were then sectioned for characterization, as shown in Figure 1(a). Due to the geometrical configuration of the casting configuration, the center plate (P2) experienced a much slower cooling rate than the two edge plates (P1 and P3), which can be attributed to the proximity to the high temperature crucible. P2 is directly below the crucible, and thus P2 is expected to be at a higher temperature in comparison to P1 and P3. This difference in cooling rates is expected to influence the resulting microstructure and chemical homogeneity of

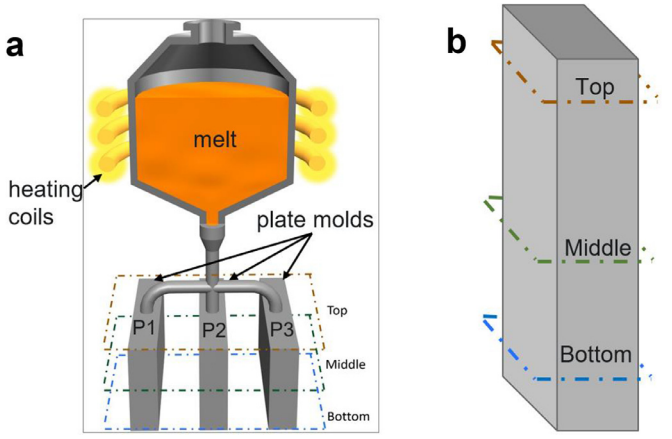


Figure 1. Schematics of (a) U-10Mo casting configuration, and (b) sectioning of cast plate for characterization. Panel (a) illustrates a single pour that yields three plates, referred to here as P1, P2, and P3.

the cast product and is discussed in later sections. Additional detail on the starting material and the fabrication process are given in Reference [27]. Here, we analyzed two different plates from a single casting. Plate 1 (P1) is one of the two side plates and Plate 2 (P2) is the center plate in the three-plate parallel-mold configuration (Figure 1(a)).

Elemental composition of the casting was measured via inductively coupled plasma mass spectrometry (ICP-MS) for top, middle, and bottom sections of two plates (P1, P2) (Figure 1(b)). The average composition for all sections was 89.57 ± 0.08 wt. % U, 10.33 ± 0.08 wt. % Mo, 257.33 ± 6.31 ppm C, 39.83 ± 6.05 ppm Si, and 358.5 ± 32.89 ppm other impurity elements. Carbon concentration before and after casting showed a ~195 ppm C pickup during the casting process.

After removing the top 5 cm (i.e., hot top) region containing slag, the as-cast plate was 24 cm long, 20 cm wide, and 0.5 cm thick. After casting and slag removal, samples were cut from the top, middle, and bottom regions (as shown in Figure 1) of the plates for characterization. Samples for characterization were sectioned using a low-speed diamond saw, mounted, and polished using conventional metallurgical sample preparation techniques [28]. Sections of U-10Mo castings were mounted in epoxy, and subsequently ground using silicon carbide (SiC) grinding papers from 180 to 1200 grit. A series of diamond suspensions (9, 3, and 1 µm) were then used to polish the surface. Samples were cleaned with deionized water and ethanol between each polishing step. The final polishing step involved placing samples on a vibratory polisher with a 0.08 µm colloidal silica polishing fluid and deionized water to obtain a fine surface finish and chemically etch the sample surface. All samples were ultrasonically cleaned after all polishing steps were completed.

Optical microscopy (OM) images were taken using an Olympus BX61 microscope to measure grain size. The grain size was estimated by measuring the grain diameters from the optical micrographs for more than 40 grains. Distribution, morphology, and composition of inclusions were analyzed using a JEOL JSM-7600F SEM equipped with an Oxford Instruments X-Max 80 EDS detector. Thresholding using Otsu's method [29] and the ImageJ software was used to estimate area fraction of inclusions as a proxy for volume fraction. Inclusions smaller than 1 μm^2 in area were not considered in these analyses. Inclusion area was calculated by measuring area of each individual inclusion, and calculating the arithmetic mean for six different SEM-BSE micrographs of 200X magnification, each with dimensions ~ 500 µm by 400 µm (200,000 μm^2). The total area of inclusions and porosities was measured

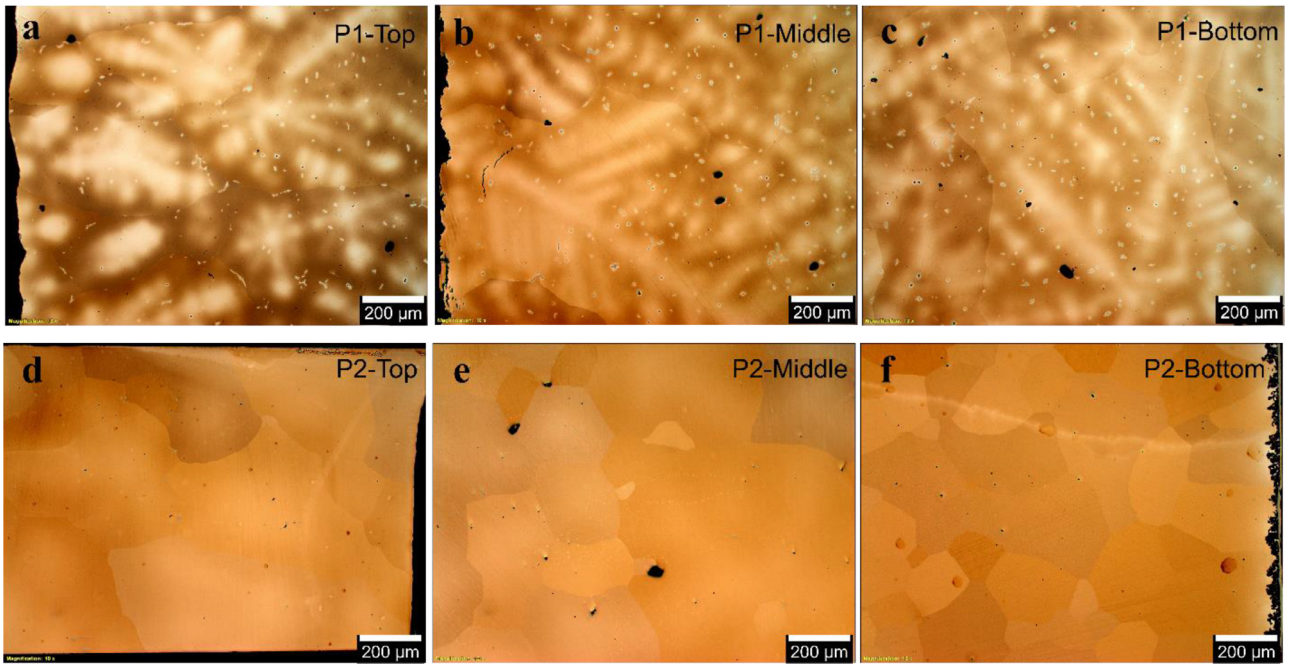


Figure 2. Optical micrographs of as-cast U-10Mo plates P1 and P2. (a) Top, (b) middle, (c) bottom regions of P1; (d) top, (e), middle, and (f) bottom regions of P2. Large black circular/oval shapes are pores.

from the BSE-SEM micrograph while the total area of the porosities was measured from the secondary electron (SE)-SEM micrographs by the thresholding method. Porosity area fraction was not included in area fraction measurements. Inclusion number density was also calculated from SEM-BSE images, according to: $\rho_{inclusions} = \frac{Total\ \#\ of\ inclusions}{Area\ of\ image}$.

Sample preparation for APT was performed using a Thermo Fisher Quanta 3-D field emission gun, focused ion beam, scanning electron microscope (FIB-SEM). Needle specimens for APT analysis were prepared using a site-specific FIB lift-out method and annular milling [30] from metallographically polished samples of as-cast U-10Mo. A CAMECA LEAP 4000X HR equipped with a 355 nm wavelength laser was used for APT data collection with the following user-selected parameters: 100 pJ laser energy, 100 kHz pulse frequency, 45 K specimen temperature, and 0.005 atoms/pulse detection rate. All data sets were analyzed using the Integrated Visualization and Analysis Software (IVAS), version 3.8.5, using manual ranging criteria. Reconstructed data sets contain a single phase (carbide, matrix, or oxide) or interface between two phases (e.g., carbide/matrix, oxide/carbide). All C concentrations were corrected according to methods detailed in prior works [14,31]. For calculating U isotopic abundances, the U species with the highest counts was used. This approach is detailed in our prior work that demonstrated calculating isotopic abundances from the major elemental peak that yielded consistent and repeatable results [14,15]. Here, for the oxide phases, no elemental peaks were detected, and hence the major oxide molecular peak was used for analyses.

3. Results

3.1. Microstructure of as-cast U-10Mo

Microstructures of plates P1 and P2 were analyzed via OM, with representative images of top, middle, and bottom sections given in Figure 2. As seen in Figure 2(a) – (c), P1 has a dendritic microstructure [33]. The dendritic structure is significantly reduced during the subsequent prolonged homogenization treatment performed at temperatures above 833 K (560°C), which is within the γ-phase field [19,34,35]. Prior work has demonstrated that after subjecting dendritic, as-cast microstructures with Mo segregation to an annealing treatment at 1074 K (800°C) for 48 hours or 1373 K (1100°C) for 16 hours, the Mo segregation is significantly reduced [34]. Hence, the dendritic microstructures seen here in sections from the P1 are expected to be removed in the subsequent homogenization annealing step performed as part of the fuel fabrication process. In contrast, Figure 2 (d) – (e) show large, equiaxed grains in plate P2, which can be attributed to the mold's position relative to the high-temperature crucible.

A closer look at the microstructure reveals a difference in contrast visible in OM images, where Mo-rich regions have bright contrast and the Mo-lean regions have a darker contrast. Hence, the Mo-lean inter-dendritic region was the last to solidify during cooling. Evidence of Mo segregation is seen in the top, middle, and bottom regions of P1 (Figure 2(a), (b), and (c), respectively); however, limited segregation can be seen in P2 sections (Figure 2(d)-(f)). The extent of Mo segregation is shown in Figure 3 from EDS line scans with 1 μm step size, taken across the entire plate cross section. Mo concentration across the top and bottom sections of P1 varies significantly: Mo is as low as ~8 wt. % in the top of the plate, and as high as ~12 wt. % in the bottom. For P2, Mo concentration is approximately constant across top and bottom sections but is higher in the bottom section (~10.5 wt. % Mo) than in the top (~9.5 wt. % Mo). The variation in the Mo concentrations in the different sections can be attributed to the differences in the cooling rates and thermal conductivity within the mold. Grain diameters measured from sections of P1 and P2 are provided as box plots in Figure 4. It was observed that average grain size in P1 was 329 μm at the top and 396 μm at the bottom, whereas in P2 the average grain diameter was 631 μm at the top, and 228 μm at the bottom.

3.2. Inclusion size and morphology

BSE-SEM micrographs were used to identify the location and distribution of the secondary-phase inclusions (i.e., uranium carbide and uranium oxide), as shown in Figure 5. These images illustrate a comparison of the three regions of P1 and P2. Evidence

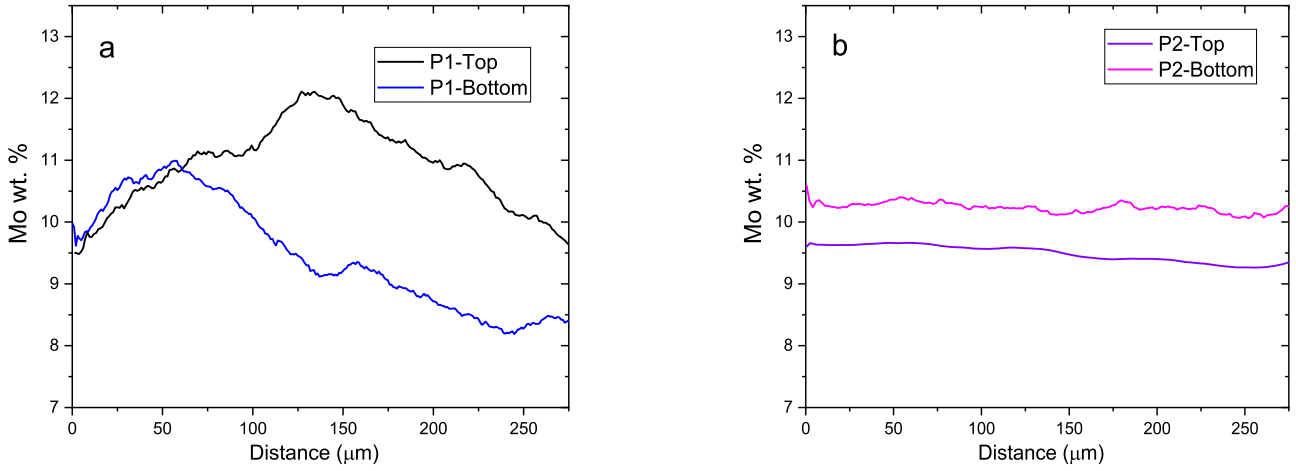


Figure 3. Mo concentration (in wt. %) across longitudinal cross sections of as-cast U-10Mo plates (a) P1 and (b) P2. Mo concentration measurements were obtained via SEM-EDS line scans with a 1 μm step size. Each profile is smoothed via averaging 20 adjacent points to illustrate the trend in composition across the plates.

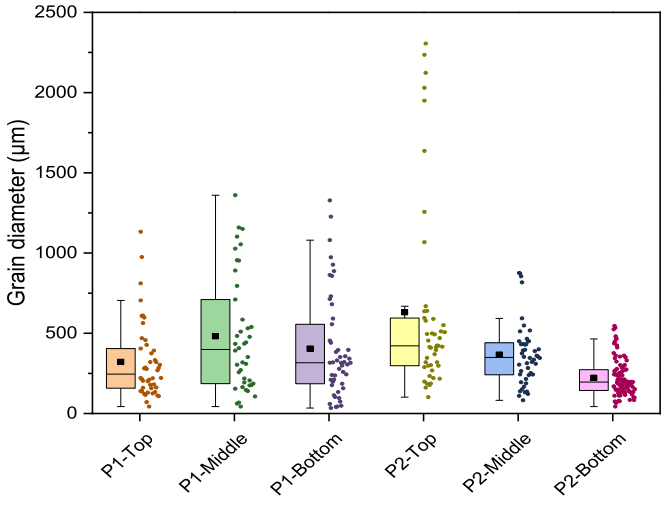


Figure 4. Grain diameter for plates 1 and 2 (P1, P2) top, middle, and bottom sections. Measured grain diameter data points are given to the right of each box-and-whisker plot. In each box and whisker plot, the median is shown as a horizontal line, the mean value as a solid square, and 25th to 75th percentiles (i.e., interquartile range, or IQR) of the data are given by the box. The whiskers indicate ± 1.5 IQR.

of microsegregation of Mo can be seen in P1 (Figure 5(a)-(c)). SEM micrographs show that the darker, dendritic core regions have higher Mo content and the brighter, interdendritic regions have lower Mo content. Microsegregation of Mo was not evident in P2 (Figure 5(d)-(f)) which can be attributed to a slower cooling rate given the higher temperature of the middle mold being closer to the crucible. Inclusions appear segregated within the interdendritic regions in P1. The inclusions may be swept toward interdendritic regions during solidification, and in some cases serve as nucleating sites for new dendrites.

The area fraction (A_f) and number density ($\rho_{inclusions} = \frac{Total\ \#\ of\ inclusions}{Area\ of\ image}$), average area, and average size of the secondary-phase inclusions are summarized in Table 1 for inclusions larger than 1 μm^2 in area. In P1, an inclusion area percentage of 0.60–0.69 % was measured, while P2 had lower values of 0.16–0.27 %. The average area percentage for both plates was 0.42 ± 0.25 %. Inclusion number density, area, and size also vary between P1 and P2, where all these parameters are greater in P1 than P2. Specifically, number density is ~247 mm^{-2} in P1 and 124 mm^{-2} in P2. Inclusion area and size follow this same trend, with ~26 μm^2 area and ~ 5 μm diameter for P1, and 18 μm^2 area and 4 μm diameter for P2.

Different inclusion morphologies were found in U-10Mo castings. Representative light micrographs of these varying morphologies are given in Figures 6 and 7 for P1 and P2, respectively. Inclusions were located at grain boundaries and in grain interiors. The grain interior inclusions have several different morphologies, many of which appear to have uniform contrast, and others that appear to have a core-shell type morphology (Figure 6(b,c,e)). Dual-phase, core-shell inclusions are observed in top, middle, and bottom regions of both castings. Inclusions observed at grain boundaries appear elongated.

Figures 6 and 7 illustrate that the overall microstructures of P1 and P2 contain similar inclusion morphologies. Further detailed analysis of inclusion composition was investigated using SEM-EDS of the center and edge of the P2 fuel plate, with results reported in Figures 8–9. The EDS maps of the P2 were used to identify regions of interest for more detailed APT analyses. From EDS mapping of the center of the fuel plate (Figure 8), we determined that the dual-phase inclusions consist of an O-rich core and a C-rich shell. The elongated, single-phase inclusions are C-rich and Mo-depleted.

In addition to the inclusions found in the center of sectioned castings, the microstructure at the edge of the P2 fuel plate was also analyzed. From SEM-BSE images and EDS mapping given in Figure 9, it is evident that the plate/mold wall interfacial layer consists of a U, Mo, and C-containing outer layer and an O-rich inner layer. The O-rich inner layer appears to be surrounded by a C-rich layer, similar to the core-shell inclusions identified in the center of the fuel plate (Figure 8).

3.3. Elemental and isotopic composition of inclusions

The elemental composition and U enrichment for both inclusions and the neighboring matrix phase was analyzed via APT to identify the point of origin of inclusions during the casting process. APT was performed for varying locations in the P2 plate. The APT mass-to-charge spectra for γ-UMo matrix, carbide, and oxide phases from as-cast LEU-Mo are given in Figure 10. The yellow highlighted regions in Figure 10 (a,c,e) indicate specific peaks in the mass-to-charge spectra used for calculating U isotopic abundance (U^{+3} peaks for matrix and carbides and UO_2^{+2} peaks for oxides). In Figure 10 (b), (d), and (f) the peaks used for U isotopic abundance calculations are shown with the ^{234}U, ^{235}U, and ^{238}U isotopes labeled.

Table 1
Summary of area percentage, inclusion number density, average inclusion area, and average inclusion size for secondary-phase inclusion in plates P1 and P2.

Sample ID	Area percentage A_f (%)	Inclusion number density, $\rho_{inclusion}$, (mm^{-2})	Average inclusion area (μm^2)	Average inclusion size (μm)
P1-Top	0.65	250	26	5.1
P1-Middle	0.69	233	29	5.4
P1-Bottom	0.60	258	23	4.8
P1 Average	*0.65*	*247*	*26*	*5.1*
P1 Standard Deviation	*0.05*	*13*	*3*	*0.3*
P2-Top	0.27	117	25	5.0
P2-Middle	0.16	88	18	4.2
P2-Bottom	0.17	167	10	3.1
P2 Average	*0.20*	*124*	*18*	*4.1*
P2 Standard Deviation	*0.06*	*40*	*8*	*1.0*
P1 and P2 Average	*0.42*	*186*	*22*	*4.6*
P1 and P2 Standard Deviation	*0.25*	*72*	*7*	*0.8*

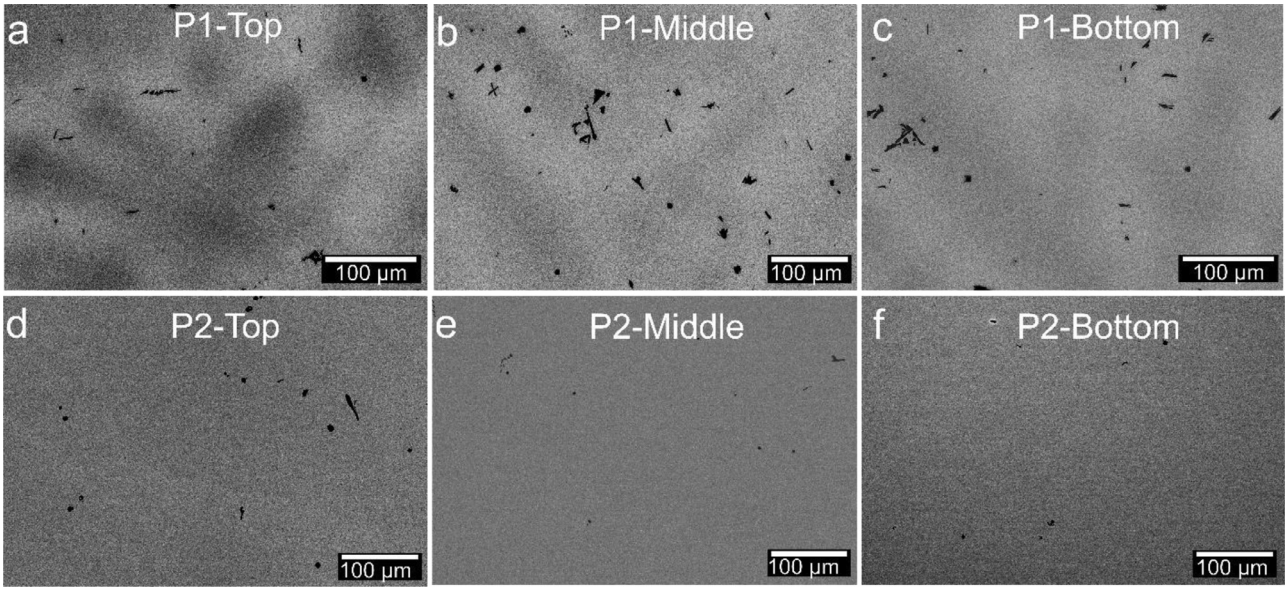


Figure 5. BSE-SEM micrographs of two plates from a U-10Mo casting. Micrographs illustrate inclusion distribution in Plate 1 (P1) (a) top, (b) middle, and (c) bottom sections, and Plate 2 (a) top, (b), middle, and (c) bottom sections.

The compositions of γ-UMo matrix, oxide, and carbide phases are summarized in Figure 11 for different locations within the casting. Inclusions were analyzed from the centers of both top and bottom sections, in addition to the edge of the sectioned plate (P2). APT analysis reveals the composition of γ-UMo matrix phase is consistent between top and bottom sections, with limited variations in alloying and impurity element concentrations. In contrast, the composition of inclusions does vary based on the location in the plate. The main differences are in the C and O concentrations of both carbides and oxides. Carbides in the top and bottom regions of the ingot have minimal O ($<$ 0.30 at. %), however, carbides in the bottom edge region have an average of ~4 at. % O. C concentration in carbides also varies from ~38 at. % (top and edge sections) to 44 at. % (bottom section). In the oxides analyzed, C concentration varied from 0 up to ~2 at. %. U oxides inclusions in the edge region also contained more C than those found in the center of the top and bottom regions. Additionally, Si content varied in each phase, from $\leq$ 0.22 at. % in γ-UMo and oxides, to ~1–3 at. % in carbides. The carbides with the highest Si concentration were found in the center of the fuel plate.

In addition to composition analysis via APT, composition changes across nanoscale microstructural features were also investigated. Specifically, elemental mappings across oxide/carbide and oxide/metal interfaces were studied, with results reported in Figures 12 and 13, respectively. APT analysis from the plate/mold interfacial layer at the P2 plate edge (Figure 12(a)-(b)) reveals spherical and elongated nanoscale oxides embedded in a hypostoichiometric carbide. The distributions of all ions, U, C, UO, and UO_2 within the APT reconstruction are given in Figure 12 (c)-(h). Up to 10 at. % O was observed inside carbides as shown in Figure 12 (i). H and Si was also observed inside carbide as highlighted in Figure 12(j). Thus, the carbide does not have UC stoichiometry, but is hypostoichiometric and therefore labeled UC_{1-x}, where x is between 0.73 and 0.13, depending on the location relative to the carbide/oxide interface. The nanoscale oxides are also hypostoichiometric (UO_{2-x}), with x between 0.02 and 0.12, owing to the presence of C, H, and Si.

APT analysis was also performed for an oxide core/carbide shell inclusion. APT samples were prepared from the center of the P2 plate, where the microstructure and region of interest used in analysis is shown in Figure 13 (a-b). APT analysis revealed the presence of an oxide/γ-UMo interface (below the sample surface), indicating that the oxide core is not completely encapsulated by a carbide shell. Figure 13 (c)-(g) show element distribution maps of U, U oxide (i.e., UO, UO_2), Mo, Si, H, and UH species, and (h) - (l) show corresponding 2D maps of U, O, Mo, Si, and H with compositional scale bars below each map. Figure 13 (m)-(n) detail compositions changes across the oxide/UMo interface across a 30 at. % O isoconcentration surface. Here, we observed Si and H enrichment (up to 3 and 9 at. %, respectively) adjacent to the oxide/metal interface. This local region of Si and H enrichment is also depleted in Mo. It is noted here that the H measurements reported (Figures 12-13) may

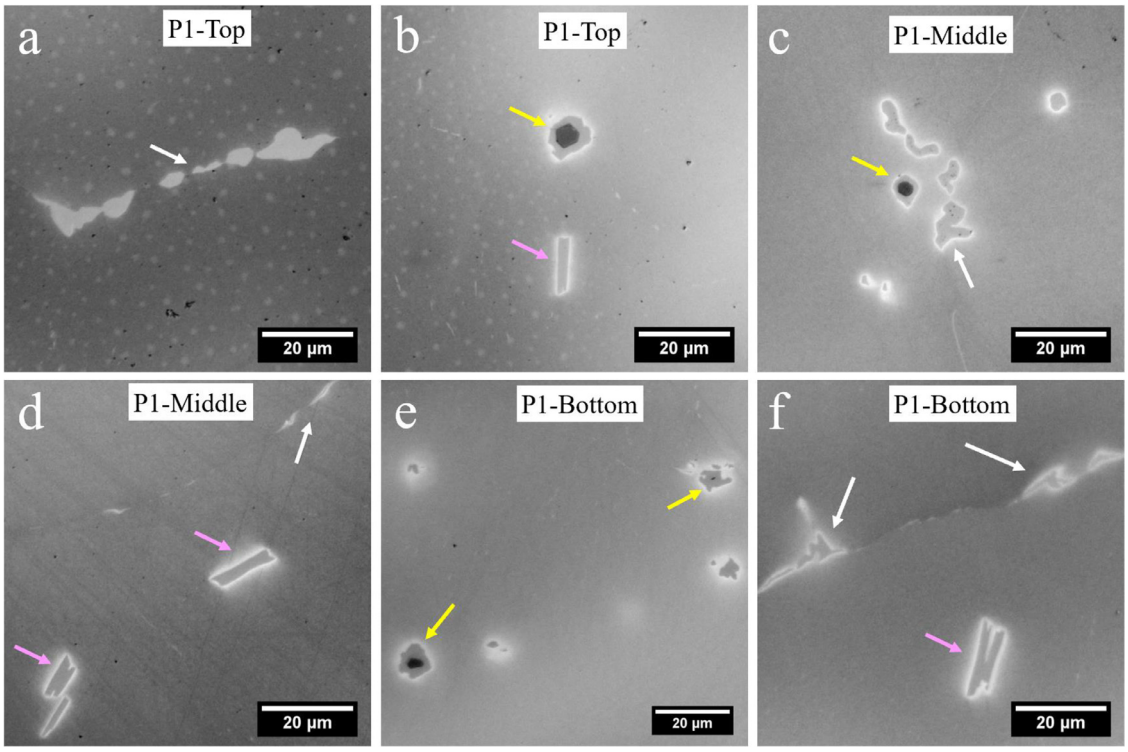


Figure 6. Representative light micrographs of secondary-phase inclusions found in U-10Mo castings for plate P1: (a,b) top, (c,d) middle, and (e,f) bottom sections. Inclusion types/morphologies are indicated by arrow color (white – grain boundary or interfacial precipitates, elongated, yellow – core/shell, pink arrow – rectangular, green arrow - porosity). Residue from colloidal silica is visible in some of the micrographs, particularly in panels (a) and (b).

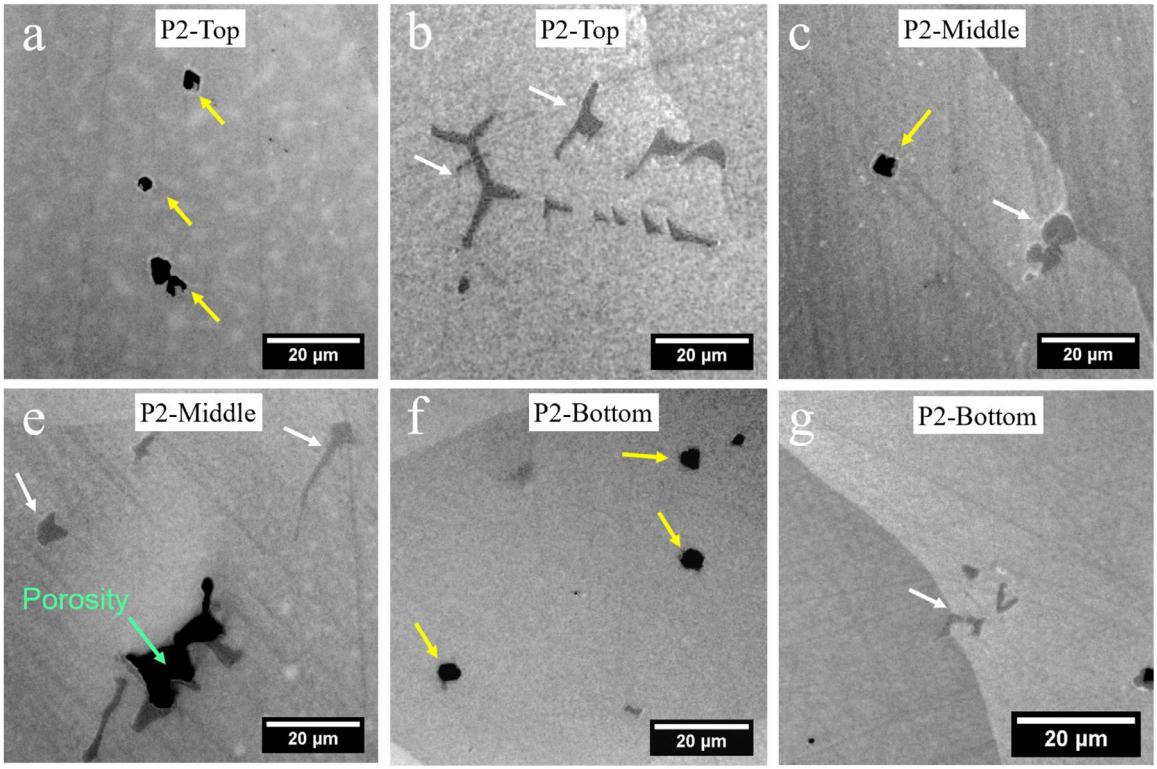


Figure 7. Representative light micrographs of secondary-phase inclusions found in U-10Mo castings for plate P2: (a,b) top, (c,d) middle, and (e,f) bottom sections. Different inclusions are indicated with colored arrows (white – grain boundary or interfacial precipitates, globular, yellow – core/shell, green arrow - porosity).

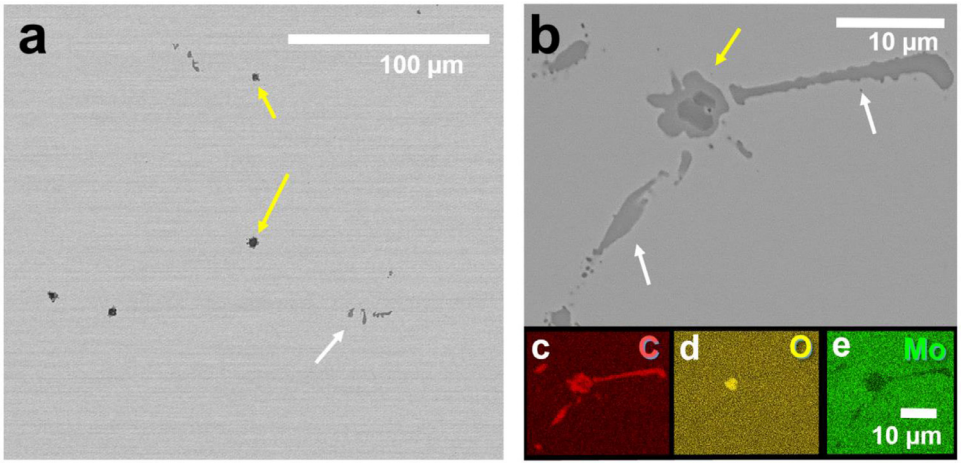


Figure 8. Microstructure of inclusions in the center of cast U-10Mo fuel plate P2: (a) representative SEM-BSE image of inclusions and matrix, and (b) a higher magnification micrograph highlighting the core-shell inclusion, with corresponding SEM-EDS maps in (c,d,e) for C, O, and Mo, respectively. Colored arrows in (a) and (b) point to different inclusion morphologies (white – globular, yellow – core/shell).

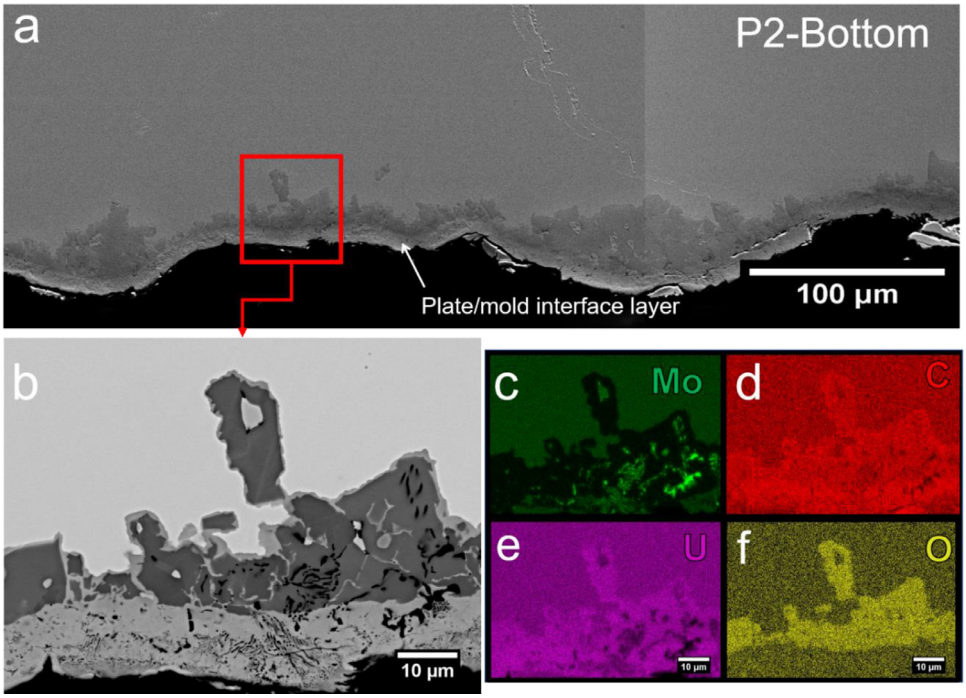


Figure 9. Microstructure of U-10Mo casting plate P2/mold interface (referred to here as the casting "edge"): (a) representative SEM-BSE image of interfacial layer, (b) a higher-magnification SEM-BSE image highlighting the details of the interfacial layer microstructure, (c,d,e) corresponding SEM-EDS maps for Mo, C, U, and O.

be impacted by several different factors, including a minor amount of residual H present in the analysis chamber, sample preparation, and user-selected parameters (e.g., pulse frequency and detection rate) [36].

While elemental compositions vary significantly between matrix and inclusion phases analyzed (Figure 11), and even within nanoscale volumes (Figures 12–13), we find U isotopic abundances are relatively consistent between phases and locations within the fuel plate, as shown in Figure 14. All U enrichments determined via APT are in close agreement with the target (~20 at. % ^{235}U), with calculated error of less than 1 at. % for all enrichment measurements (see Supplementary Information, Table S4 for details on all enrichment calculations). There is, however, slight variation in the ^{235}U percentage for some inclusions; a ^{235}U percentage slightly higher than nominal is identified in oxide inclusions in the centers of top and bottom sections of the fuel plate analyzed. This higher ^{235}U percentage suggests there are some heterogeneities in ^{235}U enrichment. Differences in enrichment between phases (i.e., carbide and matrix versus oxide) and positions in the casting (i.e., top and bottom sections versus the edge layer) can be attributed to incomplete mixing of DU and HEU feedstock.

4. Discussion

4.1. Cast fuel plate microstructures

Inclusions in U-10Mo castings were characterized across length scales using a multimodal approach to gain a detailed understanding of fuel microstructure prior to subsequent thermomechanical processing. Inclusion morphology, size, volume fraction and the elemental and isotopic compositions were studied via OM, SEM, SEM-EDS, and APT. Optical and electron micrographs indicate that

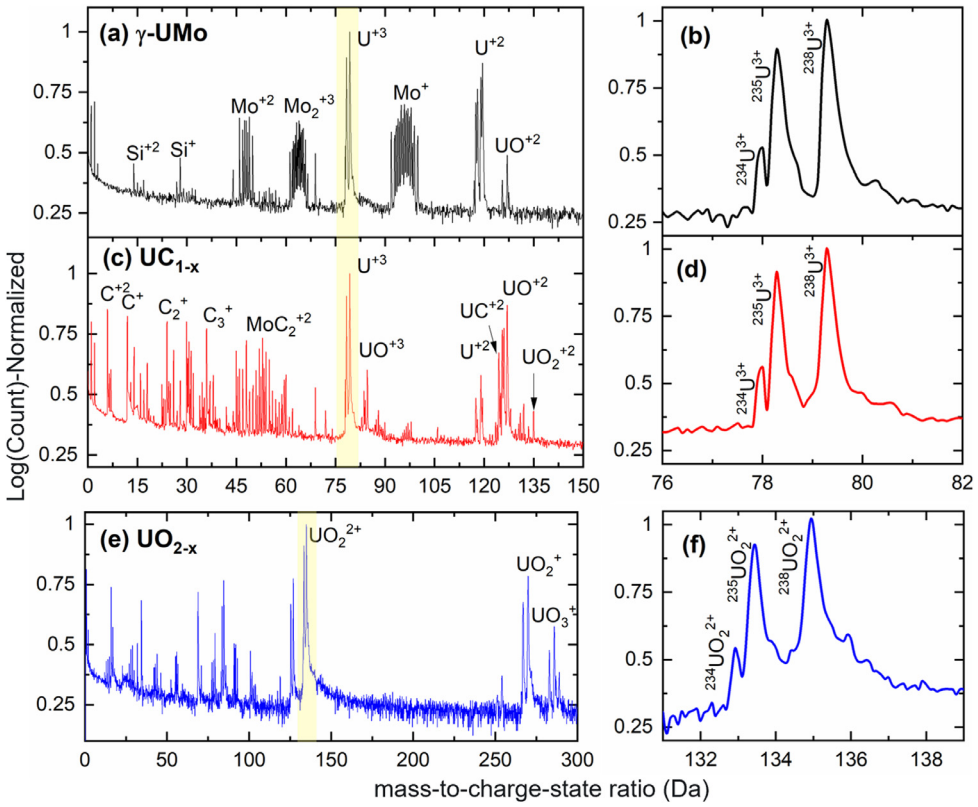


Figure 10. Representative APT mass-to-charge spectra for (a, b) γ-UMo matrix, (c,d) carbide, and (e-f) oxide phases. Complete mass-to-charge spectra are given in (a,c,e). Higher magnification views of U isotope mass-to-charge spectra peaks are given in (b,d,f). All mass spectra are plotted with a 0.1 Da bin width, and without background subtraction, as a semi-log plot.

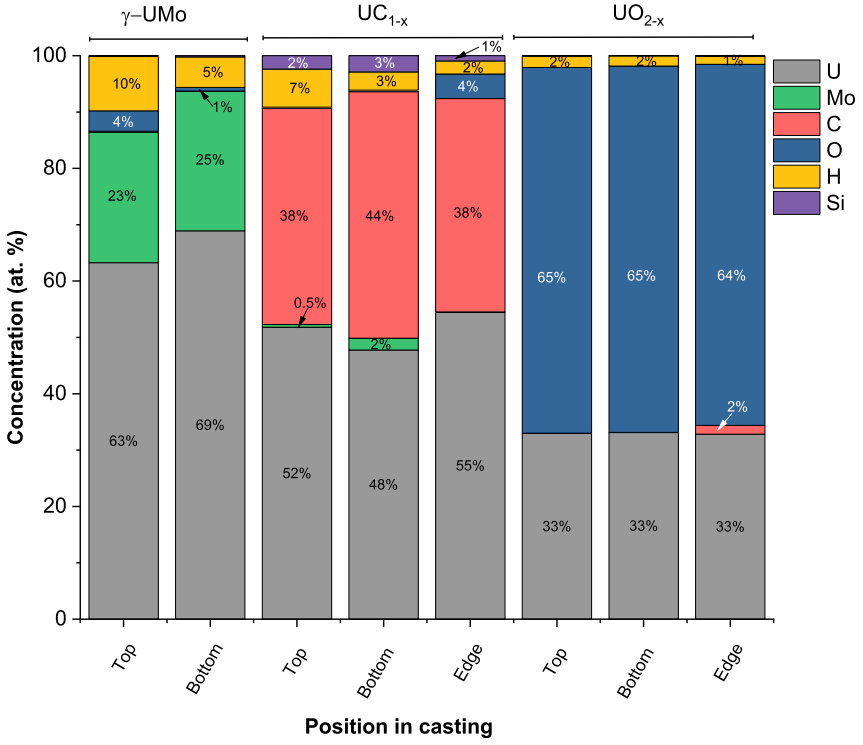


Figure 11. Composition of γ-UMo matrix, carbide, and oxide phases analyzed in different regions of a low-enriched U-10Mo casting, plate P2. Compositions reported above were determined by averaging data for each phase at each location (top, bottom, edge). The number of phases analyzed varied by position. In total, 7 volumes of γ-UMo, 6 volumes of oxide, and 6 volumes of carbide were analyzed. All raw data used to generate this plot is given in the Supplementary Information, Tables S1, S2, and S3 for matrix, oxide, and carbide phases, respectively.

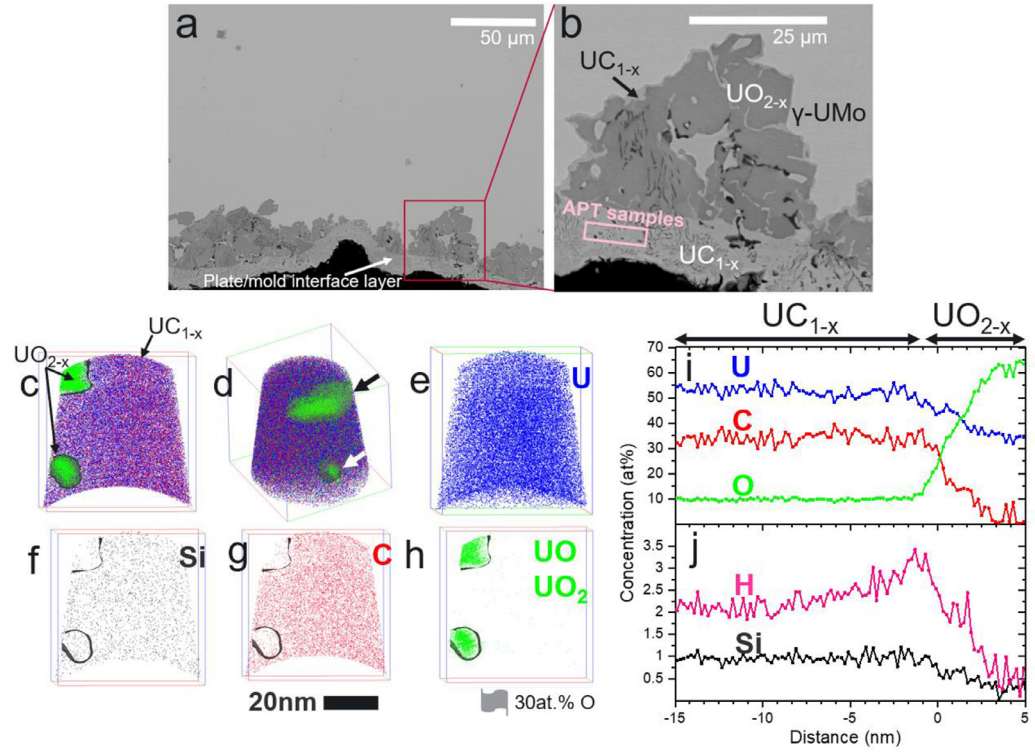


Figure 12. APT analysis of nanoscale oxides within a carbide rich interfacial layer near the U-10Mo casting edge of plate P2. The region of interest from which APT specimens were extracted and prepared is given in (a,b). 3D element distribution maps are reported for: (c,d) all ions, (e) U, (f) Si, (g) C, (h) UO and UO_2 ions. In each element distribution map, a 30 at. % O isocomposition surface (gray) is shown. A proximity histogram (with 0.2 nm bin width) across the 30 at. % O isocomposition surface is reported in (i)-(j).

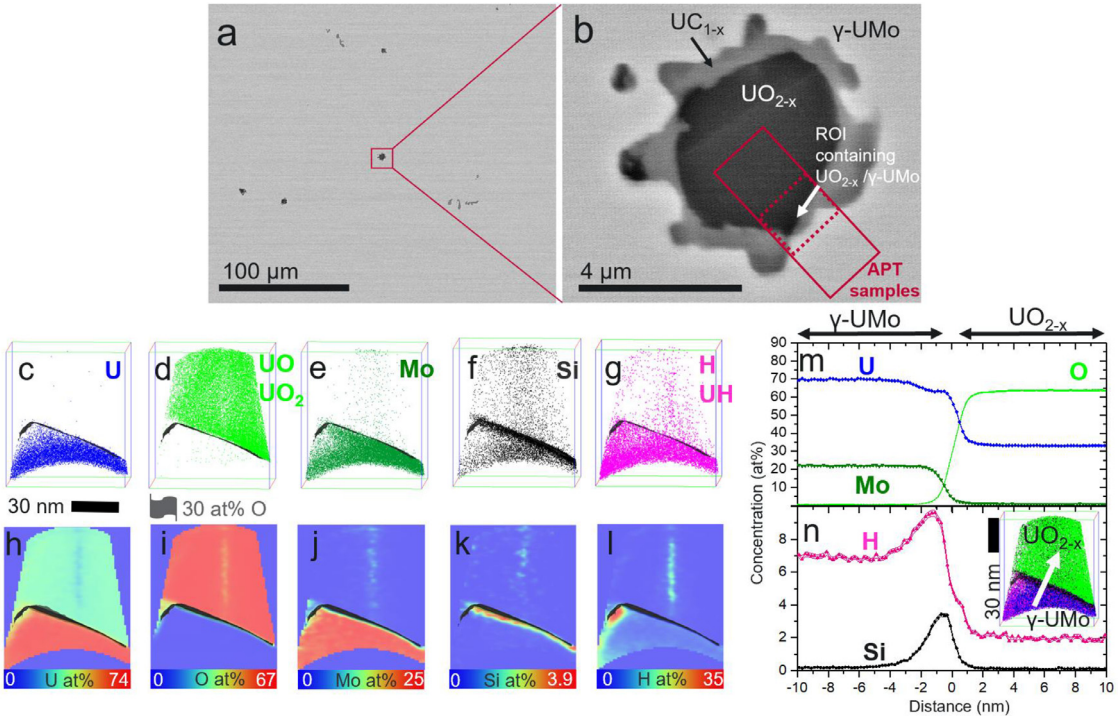


Figure 13. APT analysis of an oxide inclusion/matrix interface from the center of U-10Mo plate P2: (a,b) Region of interest from which APT needles were extracted, where 3D element distribution maps are given for (c) U, (d) U oxide species (UO, UO_2), (e) Mo, (f) Si, and (g) H, UH. Corresponding 2D contour plots are given in (h)-(l) for U, O, Mo, Si, and H, respectively. The color scale bar below each 2D contour plot provides the composition range illustrated. A proximity histogram (with 0.2 nm bin width) across a 30 at% O isocconcentration surface for U, Mo, and O is given in (m), and Si and H are plotted in (n). The inset in (n) schematically shows the direction of the profile given in (m) and (n) plots.

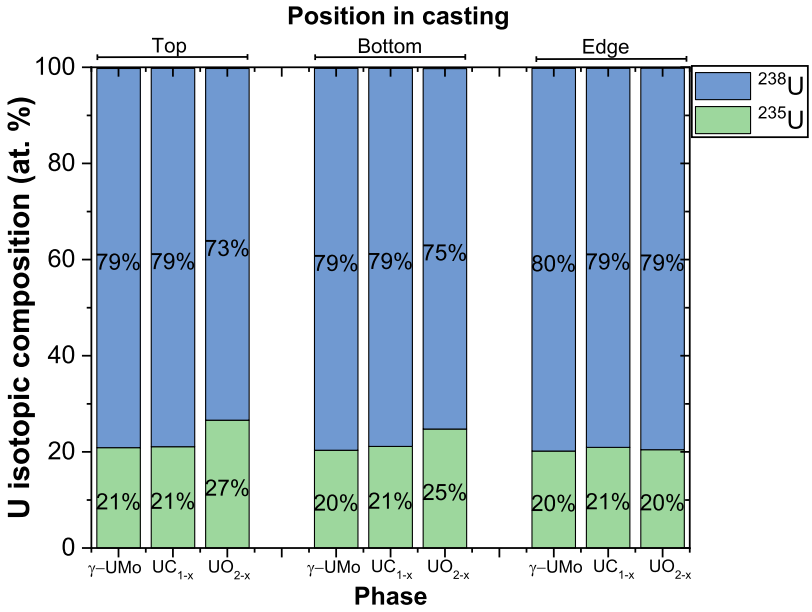


Figure 14. U isotopic composition for each position in the casting (plate P2), and phase analyzed. Percentages of ^{235}U and ^{238}U are plotted above. The ^{234}U percentage was also measured via APT, but is not shown in the graph, since it was only ~0.2 at. % for all specimens analyzed. Errors for percentages of U isotopes are less than 1 at. %, and are detailed in Supplementary Information, Table S4.

significantly different solidification and heat transfer conditions exist in two neighboring plate molds, producing dendrites in one plate (P1) and large, homogenized, equiaxed grains in the other (P2), as shown in Figure 2. The faster cooling rate in P1 (which produced a dendritic morphology) led to Mo microsegregation in the casting. In P2, large, equiaxed grains were observed after casting that arose from the much lower cooling rate, attributed to the proximity of the P2 mold to the high temperature crucible. Grain size was also found to vary between top and bottom sections of P2, where smaller grain sizes were measured at the bottom. The presence of larger grains at the top of P2 can be due to the fact that the tops of the plates were closer to the induction coils, and may have kept this region of the casting at a higher temperature. Casting molds equipped with multiple thermocouples from top to bottom of could help identify the temperature gradients and cooling rates leading to any non-uniformities in as-cast microstructures. The difference in cooling rates and heat transfer between P1 and P2 may affect microsegregation of solute atoms, and spatial variation of solute concentration in castings [37].

The area fractions and sizes of inclusions were also found to vary between P1 and P2, as detailed in Table 1. Area percentages of 0.60–0.69% and 0.16–0.27% were measured in P1 and P2, respectively, with an average of ~0.42 % considering both plates. Inclusion morphology was also investigated via light micrographs in plates P1 and P2 and similar inclusion morphologies were observed in both plates. Single- and dual-phase inclusions were both identified, and EDS mapping (performed for center and edge regions of plate P2) revealed that single-phase inclusions are C-rich, and dual-phase inclusions are comprised of an O-rich core and C-rich outer shell (referred to here as "core-shell" inclusions). In addition, an edge layer was observed, which was likely formed on the top of the casting and flowed through the vacuum induction melting crucible. Similar oxide cores surrounded by a carbide outer shell are present in this edge layer (Figure 9). Although this layer is removed after casting (prior to homogenization), knowing the composition and enrichment of this layer (and comparing it to inclusions in the center of the casting) is important for understanding how this layer was formed.

APT analysis of select inclusions (and the adjacent γ-UMo matrix phase) with varying composition and location within the top and bottom sections of P2 revealed enrichment was ~20 at. % ^{235}U. This indicates that the inclusions were formed after DU and HEU were well mixed, and the inclusions do not retain isotopic signatures from these feedstock materials. However, how and when in the casting process these impurity elements (C, O, etc.) are picked up remains unknown, although several possible pathways and experimental parameters may contribute. Several chemical reactions may lead to the formation of inclusions observed in this study, which are detailed in the subsequent sub-section.

4.2. Chemical reactions that can contribute to inclusion formation

Mechanisms contributing to O and C retention and the subsequent formation of oxides and carbides include reactions between U and carbon dioxide (CO_2), U and carbon monoxide (CO), the mold coating and graphite mold, U and graphite, and outgassing of the graphite crucible and/or coating [38,39]. If U is exposed to CO_2, then UO_2 and CO may be formed, as follows [40]:

$$U(s) + 2CO_2(g) \rightarrow UO_2(s) + 2CO(g) \quad (1)$$

U is known to readily getter CO, which can then react with liquid U, forming UC [39] according to:

$$CO(g) + 2U(l) \rightarrow UC(s) + UO(s) \quad (2)$$

CO can form during the casting process from several reactions. For example, if the Er_2O_3 coating reacts with graphite, carbon monoxide (CO) is generated [39]:

$$Er_2O_3(s) + 5C(s) \rightarrow 2ErC(s) + 3CO(g) \quad (3)$$

Another potential source of CO is from air leakage into the furnace during melting. If there are any uncoated regions of the mold, oxygen and water vapor present in air can react directly with the graphite mold, generating CO [39]:

$$O_2(g) + 2C(s) \rightarrow 2CO(g) \quad (4)$$

$$H_2O(g) + C(s) \rightarrow CO(g) + H_2(g) \quad (5)$$

Several experimental parameters can affect the extent of C pickup in U castings, including melt temperature, exposure time, and the ratio of coated crucible surface area to the mass of the molten U alloy. If CO_2 is present in the casting environment (potentially due to air leakage), U dioxide (UO_2) and UC can result according to Reactions 1 and 2, respectively. Prior work by Reiner and Holcombe found that a yttria mold coating can react with the graphite crucible, but this reaction only increased C by ~2 ppm, which did not account for all C picked up during casting [39]. Hence, other sources of C contamination were active; these were attributed to CO from air and/or water vapor leakage (Reactions 4 and 5), which could then react with molten U, leading to UC formation (according to Reaction 2). It is important to note that CO contamination can occur by two different mechanisms: reaction with the crucible and coating (Reaction 3) and air leakage (Reactions 4 - 5). If CO is generated by interaction of the mold coating with graphite, CO enters the melt at the crucible/liquid interface, whereas if CO is generated by air leakage, it reacts with molten U at the liquid/vacuum interface [39]. In both cases, the extent of the CO reaction with molten U depends on mold surface-to-melt ratio (i.e., casting surface area). Any CO reaction resulting from air leakage should also be heavily dependent on pressure at the melt/vacuum interface, and C contamination from the coating-graphite reaction may also depend on kinetics of Reactions 2 and 3 [39]. It is also noted that if air leakage does occur, and nitrogen (N) gas can be present and react with U, leading to the formation of inclusions such as UN or UN containing variable quantities of UO and UC, i.e., UN(CO) [47]. In the present work, however no evidence of a nitride phase or N in any phase was detected.

In addition to the C sources detailed above, the direct contact of molten U with the graphite crucible can also lead to the formation of UC.

Defects in the form of porosity or micro-cracks within the Er_2O_3 coating can cause a direct contact of the graphite mold with the melt locally. These defects could result either prior to or during casting. Such defects can easily go unnoticed if they are too small for them to be detected by visual inspection immediately after the coating procedure and prior to casting. The shearing forces as a result of the turbulent flow of the melt upon impact with the sidewalls and bottom of the mold can also form local defects in the coating, leading to local reactions between U melt and C from the graphite mold.

In an effort to identify the source of C pickup during casting, Reiner and Holcombe performed a parametric study investigating CO reaction with liquid U and U-Nb alloys as a function of Nb concentration, furnace time and temperature, liquid-vacuum interfacial area, and CO pressure [39]. Their results indicated that CO reaction with molten U was a major source of C contamination in cast U alloys. This study indicated that reaction kinetics were consistent with the rate-determining step being CO diffusion through an oxide film at the liquid-vacuum interface (where this oxide film was formed as a result of air leakage). The CO-U reaction was also identified as more important in C pickup than the reaction between the mold coating and graphite crucible. To reduce C in castings, parameters such as casting temperature, alloy surface area, and furnace pressure may be modified.

For the castings studied here, all these experimental parameters were approximately constant, although the actual temperature in the mold for P1 is clearly different from that for P2 (despite the temperature of the melt being the same). Tighter control of temperature in each of the three plates cast in one pour may yield more uniform C pickup across fuel plates, and also more uniform Mo distribution and equiaxed grains. The presence of agglomerated carbides and oxides on casting edges (adjacent to the plate/mold interface) suggests there is a surface reaction taking place that forms of a layer of carbides and oxides, which may slow the diffusion of C and O toward the center of the casting. The interfacial layers on the casting edge may be a result of CO reaction with the molten U-Mo. A parametric study of C pickup as a function of furnace pressure, temperature, and specific surface area of the casting for U-10Mo alloys in a prototypical casting setup may provide further insight into reaction mechanisms contributing most significantly to the C (and O) measured in these castings.

In addition to the presence of C and O, H is also enriched along the oxide/carbide and oxide/matrix interfaces (Figures 12 and 13), and may contribute to the local corrosion of carbide and metallic phases [41]. Several potential sources may contribute to this local H enrichment, where H may originate from water vapor exposure during melting, casting, or storage. The specimens studied here were also briefly exposed to water during metallographic sample polishing. Further, from Equation 5, we know that the reaction between water vapor and C may produce H gas. Considering that H may be present as a H_2 or water vapor (H_2O), reactions between these species and the U metal and U inclusions are possible and could contribute to the H enrichment observed at U metal/oxide and carbide/oxide interfaces. The stoichiometric chemical reactions describing the reaction of UC and UO_2 with water vapor are given in Equations 6 and 7 [42]:

$$UC(s) + 2H_2O\ (g) \rightarrow UO_2(s) + C(s) + 2H_2(g) \quad (6)$$

$$U(s) + 2H_2O(g) \rightarrow UO_2(s) + 2H_2(g) \quad (7)$$

Both UC and U metal can react with water vapor, forming products such as UO_2, C, and H_2. Recently, a mechanism for the corrosion of U exposed to a water vapor environment was proposed, and involves two reaction fronts: (1) between a U hydride phase (UH_3) and UO_2, and (2) between the U metal and UH_3 [43]. This proposed mechanism involves the reaction of UH_3 with OH^-, producing UO_2 and H (reaction front 1, Equation 8), and the reaction of U metal with H, producing UH_3 (reaction front 2, Equation 9 , as follows:

$$UH_3 + 2OH^- \rightarrow UO_2 + 5H + 2e^- \quad (8)$$

$$2U(s) + 3H_2(g) \rightarrow 2UH_3\ (s) \quad (9)$$

This proposed mechanism is supported by prior studies that clearly demonstrated a thin subsurface hydride/deuteride layer was present between the U oxide and metal when U metal is exposed to water vapor environments (i.e., H_2O and D_2O) [44-46]. Hydroxyl species were clearly shown in the oxide layer, and were identified as the diffusing reactant in the corrosion of U metal exposed to water vapor [45]. Although we do not find the exact stoichiometry of UH_3 in this work, the H enrichment may be early stages of hydride formation (with insufficient H available to form a hydride phase).

Given the many reactions and reaction products possible in the complex U casting process, the interaction between water vapor, gases (H_2, CO, CO_2, etc.) and U metal, oxide, and carbide phases may contribute to the formation of oxide and carbide inclusions. It is also reasonable to assume that reaction of any gases or water vapor from the environment will vary for U alloys with varying compositions and inclusion fractions. To further probe the origin of H and its role in inclusion formation and/or corrosion mechanisms of carbide and metal phases studied here, the use of isotopic tracers (e.g., deuterium) in controlled gas and water vapor environments may be instructive. Isotopic tracers may also be valuable in studying C and O pickup in these castings (e.g. ^{13}C, ^{18}O).

5. Conclusions

The microstructure of as-cast U-10Mo fuel plates, including grain size and morphology, inclusion area fraction, number density, size, and elemental and isotopic compositions, was investigated via microscopy methods across length scales (sub-nanometer to millimeter). Findings and conclusions from the work presented herein are summarized as follows:

i Cast U-10Mo fuel plate microstructures contained only small percentages of inclusions ($<$ 1 % by area). An average area percent of inclusions was measured to be ~0.4%. Average number density and area were ~171 mm^{-2} and ~22 μm^2, respectively. Inclusions have multiple morphologies (e.g., core-shell, elongated, globular, blocky) and are located at grain boundaries and grain interiors.
ii The inclusions were identified as hypostoichiometric oxides (UO_{2-x}) and carbides (UC_{1-x}) via APT analysis.
iii ^{235}U enrichment measured via APT in all phases and locations was ~ 20 at. % (consistent with nominal enrichment for LEU fuels), indicating that nonmetallic inclusions were formed in the casting process and not retained from raw materials.
iv Several possible sources of impurity elements (e.g., O, C) that can lead to formation of oxides and carbides during solidification were identified. Several pathways are possible for the production or retention of CO, CO_2, or O_2 including: (1) reaction of the U alloy with the crucible or the crucible coating, (2) exposure of the melt to trace CO_2, O_2 or H_2O from the atmosphere, and (3) small defects in the mold coating that can lead to the direct contact of the molten U with the graphite crucible.
v Local H enrichment at U oxide/carbide and oxide/metal interfaces was observed via APT. This H may originate from exposure of the melt or casting to water vapor during processing.

This study has implications for research related to the microstructural evolution of as-cast metallic fuels, where the presence of nonmetallic inclusions affects recrystallization and grain growth phenomena during fuel fabrication. The approach and results presented here also have broader significance for a wide range of nuclear nonproliferation efforts, such as processing of actinides (e.g., nuclear fuel process design, bomb reduction), and nuclear forensics, in which precise, spatial measurements of isotopic abundances are critical.

Author Contributions

E.J.K. and S.S. led manuscript writing. E.J.K. prepared all samples for APT, and performed APT data collection. E.J.K, M.F., and A.D. analyzed APT data. S.S. collected and analyzed all OM and SEM images. M.A. assisted with manuscript preparation and discussion of results. A.S.K. collected SEM images and EDS maps/line scans. A.S., V.J., and C.L. led fuel fabrication characterization efforts, and contributed to discussion of results and significance to the fuel fabrication process. All authors contributed to manuscript preparation and writing.

Funding

This work was supported by the U.S. Department of Energy (DOE) National Nuclear Security Administration. A portion of this research was performed using facilities at the Environmental Molecular Sciences Laboratory, a national scientific user facility sponsored by the DOE's Biological and Environmental Research program and located at PNNL. PNNL is operated for the U.S. DOE by Battelle Memorial Institute under Contract No. DE-AC05-76RL01830.

Declaration of Competing Interest

The authors declare that they have no known competing financial interests or personal relationships that could have appeared to influence the work reported in this paper.

Acknowledgements

The authors thank Mark Rhodes of Pacific Northwest National Laboratory (PNNL) for performing bulk metallographic sample preparation, Mr. Chad Painter for reviewing the manuscript, and Ms. Maura Zimmerschied for providing a technical review of the manuscript.

Supplementary materials

Supplementary material associated with this article can be found, in the online version, at doi:10.1016/j.jnucmat.2021.152949.

References

[1] L.C. Walters, B.R. Seidel, J.H. Kittel, Performance of Metallic Fuels and Blankets in Liquid-Metal Fast Breeder-Reactors, Nucl Technol 65 (2) (1984) 179–231.
[2] J.H. Kittel, B.R.T. Frost, J.P. Mustelier, History of fast reactor fuel development, Transactions of the American Nuclear Society 66 (1992) 174.
[3] D.E. Burkes, R.S. Fielding, D.L. Porter, D.C. Crawford, M.K. Meyer, A US perspective on fast reactor fuel fabrication technology and experience part I: metal fuels and assembly design, Journal of Nuclear Materials 389 (3) (2009) 458–469.
[4] W.A. Bostrom, M.W. Burkart, E.K. Halteman, R.D. Leggett, R.K. McGeary, T.R. Padden, Development and Properties of Uranium-Base Alloys Corrosion Resistant in High Temperature Water. Part I. Alloys without Protective Cladding, Westinghouse Electric Corp. Atomic Power Div., Pittsburgh, 1955.
[5] W.J. Carmack, D.L. Porter, Y.I. Chang, S.L. Hayes, M.K. Meyer, D.E. Burkes, C.B. Lee, T. Mizuno, F. Delage, J. Somers, Metallic fuels for advanced reactors, Journal of Nuclear Materials 392 (2) (2009) 139–150.
[6] National Academies of Sciences Engineering and MedicineReducing the Use of Highly Enriched Uranium in Civilian Research Reactors, The National Academies Press, 2016.
[7] H.A. Saller, F.A. Rough, A.A. Bauer, Transformation kinetics of uranium-molybdenum alloys, Battelle Memorial Inst., Columbus, Ohio, 1954.
[8] J. Rest, Y.S. Kim, G.L. Hofman, M.K. Meyer, S.L. Hayes, U-Mo fuels handbook. Version 1.0, Argonne National Lab.(ANL), Argonne, IL (United States), 2006.
[9] D.E. Burkes, T. Hartmann, R. Prabhakaran, J.-F. Jue, Microstructural characteristics of DU–xMo alloys with x = 7–12 wt%, Journal of Alloys and Compounds 479 (1-2) (2009) 140–147.
[10] J.E. Antill, K.A. Peakall, Oxidation of uranium alloys in carbon dioxide and air, Journal of the Less Common Metals 3 (3) (1961) 239–246.
[11] R. Prabhakaran, L. Gardner, V. Joshi, D. Burkes, C. Lavender, Effect of homogenization and hot rolling on the mechanical properties, microstructure and corrosion behavior of U-10Mo monolithic fuel, J Nucl Mater 527 (2019) 151804.
[12] L. Kovarik, A. Devaraj, C. Lavender, V. Joshi, Crystallographic and compositional analysis of impurity phase U2MoSi2C in UMo alloys, Journal of Nuclear Materials 519 (2019) 287–291.
[13] A. Devaraj, L. Kovarik, E. Kautz, B. Arey, S. Jana, C. Lavender, V. Joshi, Grain boundary engineering to control the discontinuous precipitation in multicomponent U10Mo alloy, Acta Materialia 151 (2018) 181–190.
[14] E.J. Kautz, D.E. Burkes, V.V. Joshi, C. Lavender, A. Devaraj, Nanoscale Spatially Resolved Mapping of Uranium Enrichment Scientific Reports 9 (9) (2019) 12302.
[15] E. Kautz, J. Cliff, T. Lach, D. Reilly, A. Devaraj, Correlating nanoscale secondary ion mass spectrometry and atom probe tomography analysis of uranium enrichment in metallic nuclear fuel, Analyst 146 (1) (2021) 69–74.
[16] C.D. Harrington, A.E. Ruehle, Uranium production technology, Van Nostrand, 1959.
[17] N.C. Jessen Jr., Melting and Casting of Uranium and Uranium Alloys, in: H.A. Saller (Ed.) Oak Ridge Y-12 Plant, TN (USA), Oak Ridge, Tennessee, 1982, p. 27.
[18] R. Prabhakaran, U-Mo Monolithic Fuel for Nuclear Research and Test Reactors, JOM 69 (12) (2017) 2529–2531.
[19] Z. Xu, V. Joshi, S. Hu, D. Paxton, C. Lavender, D. Burkes, Modeling the homogenization kinetics of as-cast U-10wt% Mo alloys, J Nucl Mater 471 (2016) 154–164.
[20] A.J. Clarke, K.D. Clarke, R.J. McCabe, C.T. Necker, P.A. Papin, R.D. Field, A.M. Kelly, T.J. Tucker, R.T. Forsyth, P.O. Dickerson, J.C. Foley, H. Swenson, R.M. Aikin, D.E. Dombrowski, Microstructural evolution of a uranium-10 wt.% molybdenum alloy for nuclear reactor fuels, J Nucl Mater 465 (2015) 784–792.
[21] A. Devaraj, E. Kautz, L. Kovarik, S. Jana, N. Overman, C. Lavender, V.V. Joshi, Phase transformation of metastable discontinuous precipitation products to equilibrium phases in U10Mo alloys, Scripta Materialia 156 (2018) 70–74.
[22] W.E. Frazier, S. Hu, N. Overman, C. Lavender, V.V. Joshi, Short communication on Kinetics of grain growth and particle pinning in U-10 wt.% Mo, J Nucl Mater 498 (2018) 254–258.

[23] I.S. Wani, G.D. Sathiaraj, M.Z. Ahmed, S.R. Reddy, P.P. Bhattacharjee, Evolution of microstructure and texture during thermo-mechanical processing of a two phase Al0.5CoCrFeMnNi high entropy alloy, Materials Characterization 118 (2016) 417–424.
[24] R.D. Doherty, D.A. Hughes, F.J. Humphreys, J.J. Jonas, D.J. Jensen, M.E. Kassner, W.E. King, T.R. McNelley, H.J. McQueen, A.D. Rollett, Current issues in recrystallization: a review, Materials Science and Engineering A-Structural Materials Properties Microstructure and Processing 238 (2) (1997) 219–274.
[25] Z. Jin, D. Yu, X. Wu, K. Yin, K. Yan, Drag effects of solute and second phase distributions on the grain growth kinetics of pre-extruded Mg-6Zn alloy, Journal of Materials Science & Technology 32 (12) (2016) 1260–1266.
[26] W.E. Frazier, S. Hu, V.V. Joshi, A Potts Model parameter study of particle size, Monte Carlo temperature, and "Particle-Assisted Abnormal Grain Growth, Computational Materials Science 185 (2020) 109945.
[27] A. DeMint, J. Henkel, M. Henkel, P. Hoppe, H.A. Longmire, B. Pehrson, Y-12 Naational Security Complex U-Mo Fabrication For MP-1, RERTR 2016 - 37th International Meeting on Reduced Enrichment For Research and Test Reactors, 2016.
[28] R. Prabhakaran, V.V. Joshi, M.A. Rhodes, A.L. Schemer-Kohrn, A.D. Guzman, C.A. Lavender, U-10Mo Sample Preparation and Examination using Optical and Scanning Electron Microscopy, Pacific Northwest National Lab. (PNNL), Richland, WA (United States), 2016.
[29] N. Otsu, A threshold selection method from gray-level histograms, IEEE transactions on systems, man, and cybernetics 9 (1) (1979) 62–66.
[30] A. Devaraj, D.E. Perea, J. Liu, L.M. Gordon, T.J. Prosa, P. Parikh, D.R. Diercks, S. Meher, R.P. Kolli, Y.S. Meng, S. Thevuthasan, Three-dimensional nanoscale characterisation of materials by atom probe tomography, International Materials Reviews 63 (2) (2018) 68–101.
[31] M. Thuvander, J. Weidow, J. Angseryd, L.K.L. Falk, F. Liu, M. Sonestedt, K. Stiller, H.-O. Andrén, Quantitative atom probe analysis of carbides, Ultramicroscopy 111 (6) (2011) 604–608.
[33] A.E. Dwight, The uranium-molybdenum equilibrium diagram below 900°C, J Nucl Mater 2 (1) (1960) 81–87.
[34] V.V. Joshi, E.A. Nyberg, C.A. Lavender, D. Paxton, D.E. Burkes, Thermomechanical process optimization of U-10wt% Mo – Part 2: The effect of homogenization on the mechanical properties and microstructure, J Nucl Mater 465 (2015) 710–718.
[35] E.A. Nyberg, V.V. Joshi, C.A. Lavender, D.M. Paxton, D. Burkes, Influence of Homogenization on the Mechanical Properties and Microstructure of the U-10Mo Alloy, Pacific Northwest National Lab.(PNNL), Richland, WA (United States), 2014.
[36] R.P. Kolli, Controlling residual hydrogen gas in mass spectra during pulsed laser atom probe tomography, Advanced Structural and Chemical Imaging 3 (1) (2017) 10.
[37] J. Campbell, Complete casting handbook: metal casting processes, metallurgy, techniques and design, Butterworth-Heinemann, 2015.
[38] C.E. Holcombe Jr., R.H. Reiner, N.L. Dykes, Use of Tribocor 532N for a carbon-free induction furnace for vacuum-induction melting and casting of uranium and its alloys, Journal of Materials Science Letters 6 (11) (1987) 1353–1355.
[39] R.H. Reiner, C.E. Holcombe Jr., Carbon monoxide reaction with liquid uranium-niobium alloys, Oak Ridge Y-12 Plant, TN (USA), 1986.
[40] R.J. Pearce, I. Whittle, D.A. Hilton, The oxidation of uranium in carbon dioxide and carbon monoxide (A review), Journal of Nuclear Materials 33 (1) (1969) 1–16.
[41] A. Banos, N.J. Harker, T.B. Scott, A review of uranium corrosion by hydrogen and the formation of uranium hydride, Corrosion Science 136 (2018) 129–147.
[42] T.B. Scott, J.R. Petherbridge, N.J. Harker, R.J. Ball, P.J. Heard, J. Glascott, G.C. Allen, The oxidative corrosion of carbide inclusions at the surface of uranium metal during exposure to water vapour, Journal of Hazardous Materials 195 (2011) 115–123.
[43] S.R. Monisha Natchiar, R.E. Hewitt, P.D.D. Monks, P. Morrall, Asymptotics of Coupled Reaction-Diffusion Fronts With Multiple Static and Diffusing Reactants: Uranium Oxidation in Water Vapor, SIAM Journal on Applied Mathematics 80 (5) (2020) 2249–2270.
[44] A. Banos, K.R. Hallam, T.B. Scott, Corrosion of uranium in liquid water under contained conditions with a headspace deuterium overpressure. Part 2: The ternary U + H2O(l) + D2 system, Corrosion Science 152 (2019) 261–270.
[45] T.L. Martin, C. Coe, P.a.J. Bagot, P. Morrall, G.D.W. Smith, T. Scott, M.P. Moody, Atomic-scale Studies of Uranium Oxidation and Corrosion by Water Vapour, Scientific Reports 6 (2016) 25618.
[46] A. Banos, K.R. Hallam, T.B. Scott, Corrosion of uranium in liquid water under vacuum contained conditions. Part 1: The initial binary U + H2O(l) system, Corros Sci 152 (2019) 249–260.
[47] K.E. Meredith, L.I.M. Member, M.B. Waldron, Inclusions in Uranium Metal, Journal of the Institute of MEtals 87 (1958) 311–317.